Microscopic Structural Evolution during Ultrastable Metallic Glass Formation

Peng Luo, Fan Zhu, Yu-Miao Lv, Zhen Lu, Lai-Quan Shen, Rui Zhao, Yi-Tao Sun, Gavin Vaughan, Marco Di Michiel, Beatrice Ruta, et al.

Microscopic structural evolution during ultrastable metallic glass formation

Peng Luo[1*], Fan Zhu[2], Yu-Miao Lv[1], Zhen Lu[3], Lai-Quan Shen[1], Rui Zhao[1], Yi-Tao Sun[1], Gavin Vaughan[4], Marco di Michiel[4], Beatrice Ruta[4,5], Hai-Yang Bai[1,6,7]*, and Wei-Hua Wang[1,6,7]

[1]*Institute of Physics, Chinese Academy of Sciences, Beijing 100190, China*

[2]*State Key Laboratory of Metal Matrix Composites, School of Materials Science and Engineering, Shanghai Jiao Tong University, Shanghai 200030, China*

[3]*World Premier International Research Centers Initiative (WPI), Advanced Institute for Materials Research, Tohoku University, Sendai, Japan*

[4]*ESRF-The European Synchrotron, CS 40220, 38043 Grenoble Cedex 9, France*

[5]*Univ Lyon, Université Claude Bernard Lyon 1, CNRS, Institut Lumière Matière, Villeurbanne, France*

[6]*Songshan Lake Materials Laboratory, Dongguan, Guangdong, 523808, China*

[7]*Center of Materials Science and Optoelectronics Engineering, University of Chinese Academy of Sciences, 100049 Beijing, China*

*E-mail: pengluo@iphy.ac.cn (P.L.); hybai@iphy.ac.cn (H.Y.B.)

Abstract

By decreasing the rate of physical vapor deposition, ZrCuAl metallic glass with improved stability and mechanical performances can be formed. With scanning transmission electron microscopy, we found that the glass deposited at higher rate exhibits a heterogeneous structure with compositional fluctuations at distances of a few nanometers, which gradually disappear on decreasing the deposition rate and eventually a homogeneous, featureless structure is developed approaching ultrastability. This microscopic structural evolution suggests the existence of two dynamical processes: the faster diffusion driven by the kinetic energy of the depositing atoms, which leads to nanoscale compositional fluctuations, and the slower collective rearrangements that equilibrate the deposited atoms and eliminate the compositional and structural heterogeneity.

30 **Table of Contents**

31

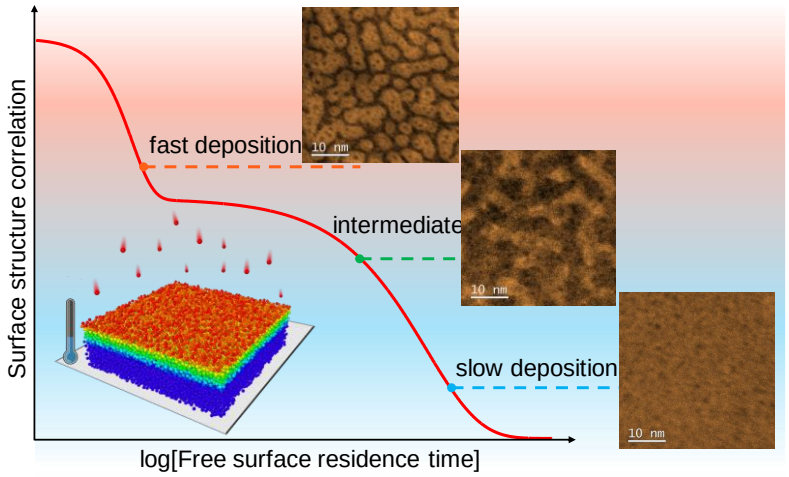

32

Unlike crystalline materials having well-defined periodic order and structural defects, the structure and property of glasses obtained from liquid quenching are generally only tunable in a limited range. In 2007 it was demonstrated that organic molecular glasses with extraordinary thermodynamic and kinetic stability[1] and exceptional mechanical and functional properties[2–5] compared to their liquid-quenched counterparts can be produced by physical vapor deposition (PVD). These glasses, termed as ultrastable glasses, have received much attention due to both their fundamental importance for understanding the nature of glass and their potentials for broad technological applications.[3–15]

In the past decades, more species of ultrastable glasses, including metallic glasses (MGs)[16,17] and polymeric glasses[18] have been fabricated by PVD, as well as Lennard-Jones glasses in computer simulations.[19] In all these works, the general consensus is that the substrate temperature (T_{sub}) during deposition is a critical variable and the optimal T_{sub} for creating an ultrastable glass is near the glass transition temperature (T_g), at 0.8~0.9T_g,[16–21] associated with the enhanced surface mobility that gives rise to a more relaxed structure.[22]

Very recently, it was found that ultrastable MGs with substantial T_g enhancement can be fabricated by PVD on room temperature substrates corresponding to $T_{sub} \approx 0.43T_g$, with reduced deposition rate (R).[23,24] Moreover, molecular dynamics (MD) simulations[25] revealed that the optimal T_{sub} for the formation of ultrastable $Zr_{49}Cu_{45}Al_6$ MG is $0.625T_g$ at constant R, already far below the empirical 0.8~0.9T_g. These findings suggest that the surface atoms of MGs retain high mobility even at low temperatures.[24] However, the microscopic structural and dynamical processes occurring in the material on approaching ultrastability is still unclear. As a multicomponent material with non-directional metallic bonds, the micromechanisms relevant to ultrastable MG formation are intrinsically challenging.

In this letter, we investigated the microscopic structure evolution of a prototypical $Zr_{46}Cu_{46}Al_8$ (at.%) MG prepared by PVD with different deposition rates, combining spherical aberration corrected scanning transmission electron microscopy (Cs-STEM) and high-energy synchrotron X-ray diffraction (XRD). The results reveal the gradual

transformation from a nanoscale heterogeneous structure to a homogeneous one with concomitant increasing prevalence of Zr-Zr bonds on decreasing *R*, providing novel insights on the microscopic processes relevant to ultrastable MG formation.

The MGs were prepared by single-target ion beam deposition without heating the substrates. More details for sample preparation and characterizations are included in the Experimental Methods. The samples were firstly examined by in-house XRD, which reveals diffuse patterns indicative of fully amorphous structure (see Fig. S1 in the Supporting Information). The Differential scanning calorimetry (DSC) curves adapted from our previous work[24] are shown in Fig. 1(a). For the glass deposited at 5.7 nm min^{-1}, T_g is measured to be 706 K, close to that of the liquid-quenched ordinary glass (698 K).[24] When *R* is lowered to 2.8 nm min^{-1}, T_g increases to 724 K. For the glass deposited at the slowest rate of 0.8 nm min^{-1}, T_g reaches 757 K. These results indicate the evolution towards ultrastable glass state through reducing *R*.

An instrumented nanoindentation is employed to examine the mechanical performances of the vapor-deposited MG films. The samples were deposited on Si(001) substrates to a thickness of 2 μm, with root mean square roughness less than 0.2 nm independent of *R* (Fig. S2). Such good surface quality eliminates the possible effects of surface defects and roughness on nanoindentation measurements. With sequential nanoindentation tests, indentation size effect[26,27] is observed at small contact depth (h < 150 nm), and substrate effect[28,29] shows up when h is larger than 200 nm (Fig. S3). To circumvent these effects, we chose a peak load of 5 mN that yields a penetration depth around 180-200 nm. The inset in Fig. 1(b) displays the representative nanoindentation load-depth curves. The lower *R*, the smaller penetration depth is under the same load, thus higher resistance against deformation. The hardness and Young's modulus evaluated by Olive-Pharr method[30] show the same deposition rate dependence as T_g [Fig. 1(b)]. As *R* decreases from 5.7 nm min^{-1} to 0.8 nm min^{-1}, the hardness and Young's modulus increase from, respectively, 126.40±1.71 GPa and 6.71±0.14 GPa to 139.48±1.36 GPa and 7.48±0.05 GPa, by ≈11%. These results demonstrate that the mechanical performances can be substantially improved with slower deposition, in good agreement with the T_g enhancement.

Figure 2 shows the high-resolution transmission electron microscopy (HRTEM) and high-angle annular dark-field STEM (HAADF-STEM) images of the MGs deposited at different rates, and the liquid-quenched MG for comparison. The homogeneous maze-like patterns in the HRTEM micrographs and the diffuse halo of the selected area electron diffraction (SAED) patterns reveal typical amorphous structure [Fig. 2(a-d)]. While no discernible difference between these samples is observed with HRTEM and electron diffraction [Fig. 2(a-d)], HAADF-STEM which is sensitive to the local chemistry and density (atomic configuration) reveals an intriguing microstructure which is strongly dependent on R [Fig. 2(e-g)]. The MG film deposited at 5.7 nm min^{-1} shows a highly heterogeneous morphology [Fig. 2(e)], consisting of mixed equiaxed and columnar domains about 4-10 nm separated by ≈1~2 nm thick boundaries with distinct contrast. As R is lowered to 2.8 nm min^{-1}, the darker boundaries expand outward and become more fuzzy while the brighter domains become, accordingly, smaller in size and less in amount. At the same time the contrast difference between these two structures decreases [Fig. 2(f)]. Eventually, at R = 0.8 nm min^{-1} this dual-phase nanostructure disappears, and a homogeneous, featureless morphology is observed [Fig. 2(g)].

The heterogeneous contrast in the STEM images implies an inhomogeneous distribution of chemistry and/or density. As shown in Fig. 3(a-d), STEM energy-dispersive X-ray spectroscopy (EDS) mapping for the 0.8 nm min^{-1} deposited MG indicates the absence of chemical fluctuation for all three elements, consistent with the uniform STEM morphology [Fig. 2(g)]. In contrast, the 5.7 nm min^{-1} deposited MG shows remarkable chemical fluctuations. While the distribution of Al atoms is uniform [Fig. 3(h)], those of Zr and Cu atoms are heterogeneous [Fig. 3(f,g)]. The brighter regions in the STEM image are enriched in Cu with, accordingly, less Zr, and the darker regions are enriched in Zr with less Cu. These results indicate that the heterogeneous structure observed in the faster deposited MGs is related to compositional fluctuations, which diminish with decreasing R and eventually disappear at the slowest deposition at 0.8 nm min^{-1}. The liquid-quenched MG should not have decomposition, hence, the heterogeneous structure at much smaller length scales (≈2 nm) [Fig. 2(h)] indicates

the presence of local atomic configuration variations as usually observed in liquid-quenched MGs.[31] The visibly more homogenous structure of the 0.8 nm min^{-1} deposited ultrastable MG [Fig. 2(g)], suggests the absence of both compositional fluctuation and obvious structural heterogeneity.

Nanoscale phase separation in ZrCu MGs has been reported first in MGs prepared by PVD at R = 30~60 nm min^{-1} by Barbee et al.[32] However, contradictory results were observed on the occurrence of phase separation in liquid-quenched ZrCu(Al) MGs.[33] Here, our observation of nanoscale phase separation in ZrCuAl MGs prepared by PVD strengthens the idea that PVD is less effective in suppressing phase separation compared to liquid quenching.[32] For ZrCu and ZrCuAl MGs containing no atom pair with positive heat of mixing (Table S1),[34] phase separation is thermodynamically unfavored and thus metastable. Figure 2(e-g) reveal the gradual transformation from a phase-separated nanostructure to a single-phase structure upon decreasing R. As R is the only variable for the sample preparation, these observations can be ascribed to the different surface residence time of the deposited atoms before being buried deeper, where their dynamics are orders of magnitude slower. Therefore, our results suggest that the depositing atoms experience two dynamic processes after arriving at the substrate: the faster diffusion process that leads to nanoscale compositional fluctuations and the slower collective rearrangements that equilibrate the deposited atoms and eliminate the compositional and structural heterogeneity.

During vapor-deposition, individual atom species are deposited onto the substrate, as the deposition parameters were maintained constant and the substrates were rotating at a constant speed (15 r/min), a uniform deposition process is expected. For all deposited MGs, atomically smooth surfaces are obtained independent of R (Fig. S2), indicating the absence of transition in growth modes.[35] In a recent experimental and simulation study on vapor-deposited atomically thin MG membranes, it was found that after arriving at the substrate the atoms aggregate to form a fractal structure on a length scale comparable to the phase separations of our observation.[36] On the other hand, our results and those of Barbee et al[32] indicate that phase separation is pronounced at higher R. Therefore, it can be concluded that the phase separation in vapor-deposited ZrCu(Al)

MGs occurs rapidly during the aggregation process, driven by the kinetic energy of the depositing atoms. However, for ZrCu(Al) MGs with negative heat of mixing (Table S1),[34] a homogeneous structure without decomposition is thermodynamically more favored.[33] Hence, with longer surface residence time allowed by slower deposition, the deposited atoms can undergo further rearrangements driving the glass towards homogenization, during which the atoms will adopt more stable structural configurations.

More detailed structural difference between the vapor-deposited MGs at different rates and the liquid-quenched MG were revealed by high-energy synchrotron XRD. Figure 4(a) displays the pair distribution functions (PDF), $G(r)$, derived from the synchrotron XRD patterns [the inset in Fig. 4(a)]. Due to the different thickness of the vapor-deposited MG films and the liquid-quenched MG ribbon, their scattering signal and the calculated $G(r)$ have different intensity, hence, for better comparison the $G(r)$ functions were normalized by their first peak maximum. Figure 4(b) shows the zoomed-in first peaks together with the interatomic distance and weight factor of the atomic pairs (Table S1). The first peaks split into a sub-peak located at r = 2.82 Å and a shoulder around 3.20 Å due to the discrete bonding length distribution of the nearest-neighbor atoms. According to the interatomic distances and weight factors, Cu-Cu, Zr-Cu and Zr-Zr atom pairs dominate the first peak. The sub-peak at 2.82 Å can be assigned mainly to Zr-Cu pairs, while the shoulder around 3.20 Å originates mostly from Zr-Zr pairs. The PDF of the 4.4 nm min^{-1} deposited MG basically overlap that of the liquid-quenched MG, while at 3.0 Å < r < 3.5 Å the 0.8 nm min^{-1} deposited MG exhibits higher $G(r)_{\text{Zr-Zr}}/G(r)_{\text{Zr-Cu}}$ ratio. This indicates more Zr-Zr pairs and lesser Zr-Cu pairs in the ultrastable MG, in agreement with previous results from MD simulation.[25] Since the heat of mixing between Zr and Cu is negative, the occurrence of phase separation does not mean an increase in the like near-neighbor pairs (Zr-Zr and Cu-Cu) and a decrease in the unlike near-neighbor pair (Zr-Cu), in agreement with our results.

Based on the model of local configurational excitations in the atomic connectivity network proposed by Egami and co-workers[37], and the experimental fact of the much slower diffusion of Zr atoms than the other atoms in liquid alloy,[38] it was proposed

that Zr atoms form significantly stronger temporary nearest-neighbor bonds that have to be broken by thermal activation than the other atoms.[38] The observation of increased prevalence of Zr-Zr bonds in ultrastable MGs in our experiments and previous MD simulations[25] further confirms this presumption and reveals the importance of Zr-Zr bonds in strengthening the atomic connectivity and enhancing the stability of MGs.

Figure 4(c) and (d) indicate that the $G(r)$ oscillations beyond the nearest-neighbor are smaller in the vapor-deposited MGs than in the liquid-quenched MG. In particular, well-defined correlation peaks till r = 22 Å are seen in the latter, while no discernable oscillations can be observed in the 4.4 nm min^{-1} deposited MG above r = 16 Å [Fig. 4(d)]. For the 0.8 nm min^{-1} deposited MG, the $G(r)$ peaks are stronger than that deposited at 4.4 nm min^{-1} and retained to larger distance around r = 18 Å. This increased medium-range ordering on decreasing R is consistent with the increased compositional and structural homogeneity in the vapor-deposited MGs (Fig. 2), but even at the slowest deposition, medium-range ordering comparable to the liquid-quenched MG is not developed in the vapor-deposited MGs, suggesting the intrinsic difference between these two glass forming paths experiencing or not the liquid state.

By looking at the heat flow curves in Fig. 1(a), an inflection is observed between T_g and the crystallization temperature (T_x) in the 5.7 nm min^{-1} deposited MG, which becomes less obvious in the 2.8 nm min^{-1} deposited MG and eventually disappears in the 0.8 nm min^{-1} deposited ultrastable MG. This is more observable in the derivatives of the heat flow (see Fig. S4). Such a deposition rate dependent two-stage-like endothermic behavior is in agreement with the chemical ordering (phase separation) of the glass as revealed by STEM [Fig. 2(e-g)]. On the other hand, it has been shown in our previous work[24] that, while the T_g of the vapor-deposited MGs is always larger than that of the liquid-quenched MG the T_x of the MG deposited at $R \lesssim 2$ nm min^{-1} is even lower than that of the liquid-quenched MG. This is analogous to the previous observation that vapor-deposited, phase-separated ZrCu MG shows lower T_x than that of liquid-quenched, single-phase MG.[32] Hence, our results confirm this phenomenon and further demonstrate that with reduced phase separation by lowering R the T_x of the vapor-deposited MG will increase and become less different from that of the liquid-

quenched, single-phase MG. These results suggest that the development of phase separation during vapor-deposition of materials with negative heat of mixing could be thermodynamically related to the propensity to crystallize of the depositing atoms having remnant kinetic energy.

These experimental facts shed new lights on the microscopic processes the atoms experience before achieving ultrastable state. After arriving at the substrate, the kinetic energy of the depositing atoms enables their faster diffusion towards the development of nanoscale chemical ordering. If the deposition is slow, long free surface residence time is allowed and the atoms undergo surface-mediated equilibration, during which both the compositional and the structural fluctuations will be eliminated as they are not thermodynamically favored for an amorphous system with negative heat of mixing, at the same time the atoms can adopt more stable structural configurations. The increased structural homogeneity with less soft sites and the strengthened atomic network with increased prevalence of Zr-Zr bonds make the glass stronger against deformation [Fig. 1(b)]. The herein observed structural and chemical homogenization may also account for the recent observations of reduced nanoscale elasticity fluctuations in ultrastable MGs.[23,39]

The changed local structure leads to increased kinetic stability as manifested by the enhanced T_g, but differently from molecular systems[40] and aged MGs,[41] on the DSC up-scans no discernable enthalpy recovery following glass transition is observed for ultrastable MGs in the present or the previous studies.[16,17,23,24] The absence of enthalpy recovery above T_g and the experimental fact that ultrastable MGs are more resistant against crystallization[23,24] suggest that the local structure modification cannot be erased before crystallization sets in. Therefore, the total amount of enthalpy change (ΔH), during heating from glassy state to fully crystallized state can reflect the energy state of the glass. Compared to the liquid-quenched MG, this enthalpy change in the vapor-deposited MGs is much less and exhibits a continuous decrease with lower R [Fig. S5]. If not considering the difference between the potential energy of the crystallization phases[23,24], the reduced ΔH roughly indicates the increased thermodynamic stability of ultrastable MGs.

To summarize, combining start-of-the-art structure characterizations, we revealed that MGs prepared by fast vapor-deposition show highly heterogeneous structure with nanoscale compositional fluctuations, which gradually transform into a homogeneous, featureless structure accompanied by increased prevalence of Zr-Zr atom pairs on decreasing R. This observations explain the inflections on the DSC curves above T_g and the reduced T_x of the MGs deposited at $R \lesssim 2$ nm min^{-1},[24] and suggest that two dynamical processes are responsible for the microscopic structural evolution: the faster diffusion driven by the kinetic energy of the depositing atoms, which leads to nanoscale compositional fluctuations, and the slower collective rearrangements that equilibrate the deposited atoms and eliminate the compositional and structural heterogeneity.

EXPERIMENTAL METHODS

Preparation of metallic glasses

MG films were prepared by ion beam deposition using a high purity $Zr_{46}Cu_{46}Al_8$ alloy target 100 mm in diameter. To remove the oxide layer on the target surface, pre-sputtering was carried out for 200 s. Prior to the deposition of the MG, 100 nm thick Aluminum was deposited on a flat polycarbonate (PC) substrate 12 cm in diameter. During the deposition, the substrate is rotated at a constant rotating speed (15 r/min), making a uniform deposition process. The ion beam energy was 750 eV. The deposition rate was controlled by the ion beam current. The base pressure of the chamber was better than 2×10^{-4} Pa. Argon was used as gas species under an operation pressure of 2.4×10^{-2} Pa. The as-received films were detached from the PC substrates by dissolving the in-between Aluminum layer in 1 mol L^{-1} NaOH solution, and then the films were cleaned by deionized water. The nanoindentation samples (2 μm thick) were directly deposited on Si(001) substrates. Ordinary MG ribbons (20 μm thick) were produced by melt-spinning technique for comparison.

Calorimetric characterization

DSC measurements for the vapor-deposited MGs were performed on a Perkin-Elmer DSC 8000 at a heating rate of 20 K min^{-1} with 20 mL min^{-1} flowing pure argon gas to prevent surface oxidation. The mass of the DSC samples is 15~20 mg to achieve

good data accuracy. Prior to measurements, the DSC was calibrated with standard samples In and Zn.

X-ray diffraction

The amorphous structure of the as-deposited films was firstly checked with a Bruker D8 Advance XRD using a Cu K_α source in the Bragg-Brentano geometry. High-energy synchrotron XRD measurements were carried out with an incoming beam energy of 79.5 keV on the ID15A beamline at ESRF, Grenoble (France). At 79.5 keV, the calculated X-ray attenuation for the 2 μm thick glass films varies from 0.17% at q = 0 Å^{-1} to 0.24% at q_{max} = 30 Å^{-1} (q is the wavevector transfer). The calculated value for the 20 μm thick ribbon varies instead from 1.7% at q = 0 Å^{-1} to 2.4% at q_{max} = 30 Å^{-1}. The attenuation is therefore linearly proportional to the sample thickness, weakly dependent on q, very small, and consequently negligible. The diffraction signal is also linearly proportional to the sample thickness. For such reasons, it is not necessary to use samples of similar thickness.

The incident flux normalization is done with a diode placed in front of the sample. Diffraction patterns were collected in transmission geometry by using a Pilatus3 X CdTe 2M hybrid photon counting detector. The detector was off-centered with respect to the incident beam and located close to the sample to access up to $q \approx 30$ Å^{-1} and to be able to calculate with a good resolution the $G(r)$ functions. The intensity profiles were corrected for the background contribution, polarization of the X-rays and detector geometrical correction. The $G(r)$ functions were calculated using routines from the Diffpy-CMI library[42] with some local modifications for outlier rejection and treatment of background effects.

Transmission electron microscopy and energy dispersive spectroscopy

Specimens for the TEM characterizations were prepared by gentle ion milling with 3 keV Argon ions at the liquid nitrogen temperature. HRTEM and HAADF-STEM observations were conducted using a cold field emission TEM (JEM-ARM200F, JEOL) equipped with a spherical aberration (Cs) corrector for the probe-forming objective lens. Preparation of TEM specimens sometimes leads to inhomogeneous thinning, making possible artifacts confused with the intrinsic microstructures.[43] According to Refs.,[31,43]

our preparation of the TEM specimens for the studied MG system is not expected to induce any artifacts.

EDS mappings were recorded at STEM mode to characterize the compositional distribution. For the 0.8 nm min^{-1} deposited MG, the EDS mapping was performed on the JEM-ARM200F Cs-STEM. The STEM image shown in Fig. 3(a) was taken at the same region of the EDS mapping. For the 5.7 nm min^{-1} deposited MG, another Cs-STEM instrument (JEM-2100F, JEOL, 200 kV) was employed at the same operation conditions. The STEM image shown in Fig. 3(e) was the morphology trace during the EDS mapping, therefore, it has lower resolution than Fig. 3(a).

Nanoindentation

The hardness and elastic modulus were characterized by nanoindentation with a diamond Berkovich indenter on a Nanoindenter G200 XP system (Skysight, USA). The force resolution and vertical displacement resolution are 50 nN and < 0.01 nm, respectively. The MGs for nanoindentation tests were deposited on Si(001) substrates to a thickness of 2 μm. Prior to the beginning of tests, the contact area function was calibrated using a standard fused silica material. The indentations were performed under a load-control mode with a maximum load of 5 mN and at a loading-unloading rate of 1 mN s^{-1}. The load was held for a period of 5 s at the peak load before unloading. The allowable drift rate is 0.05 nm s^{-1}. Six indents were made for each sample to verify the accuracy and scatter of the indentation data.

Supporting Information

The Supporting Information is available free of charge at

Figure S1-S5

Table S1

Acknowledgements

This research was supported by the Strategic Priority Research Program of the Chinese Academy of Sciences (No. XDB30000000), National Key Research and Development Plan (No. 2018YFA0703603), National Natural Science Foundation of China (Nos.

61888102 and 11790291), and Natural Science Foundation of Guangdong Province (No. 2019B030302010). Y.T.S was supported by National Natural Science Foundation of China (Grant No.51801230).

References

(1) Swallen, S. F.; Kearns, K. L.; Mapes, M. K.; Kim, Y. S.; McMahon, R. J.; Ediger, M. D.; Wu, T.; Yu, L.; Satija, S. Organic Glasses with Exceptional Thermodynamic and Kinetic Stability. *Science.* **2007**, *315* (5810), 353–356. https://doi.org/10.1126/science.1135795.

(2) Kearns, K. L.; Still, T.; Fytas, G.; Ediger, M. D. High-Modulus Organic Glasses Prepared by Physical Vapor Deposition. *Adv. Mater.* **2010**, *22* (1), 39–42. https://doi.org/10.1002/adma.200901673.

(3) Gujral, A.; O'Hara, K. A.; Toney, M. F.; Chabinyc, M. L.; Ediger, M. D. Structural Characterization of Vapor-Deposited Glasses of an Organic Hole Transport Material with X-Ray Scattering. *Chem. Mater.* **2015**, *27* (9), 3341–3348. https://doi.org/10.1021/acs.chemmater.5b00583.

(4) Ràfols-Ribé, J.; Will, P.-A.; Hänisch, C.; Gonzalez-Silveira, M.; Lenk, S.; Rodríguez-Viejo, J.; Reineke, S. High-Performance Organic Light-Emitting Diodes Comprising Ultrastable Glass Layers. *Sci. Adv.* **2018**, *4* (5), eaar8332. https://doi.org/10.1126/sciadv.aar8332.

(5) Dalal, S. S.; Walters, D. M.; Lyubimov, I.; de Pablo, J. J.; Ediger, M. D. Tunable Molecular Orientation and Elevated Thermal Stability of Vapor-Deposited Organic Semiconductors. *Proc. Natl. Acad. Sci.* **2015**, *112* (14), 4227–4232. https://doi.org/10.1073/pnas.1421042112.

(6) Léonard, S.; Harrowell, P. Macroscopic Facilitation of Glassy Relaxation Kinetics: Ultrastable Glass Films with Frontlike Thermal Response. *J. Chem. Phys.* **2010**, *133* (24), 244502. https://doi.org/10.1063/1.3511721.

(7) Vila-Costa, A.; Ràfols-Ribé, J.; González-Silveira, M.; Lopeandia, A. F.; Abad-Muñoz, L.; Rodríguez-Viejo, J. Nucleation and Growth of the Supercooled Liquid Phase Control Glass Transition in Bulk Ultrastable Glasses. *Phys. Rev.*

Lett. **2020**, *124* (7), 076002. https://doi.org/10.1103/PhysRevLett.124.076002.

(8) Rodríguez-Tinoco, C.; Gonzalez-Silveira, M.; Ràfols-Ribé, J.; Vila-Costa, A.; Martinez-Garcia, J. C.; Rodríguez-Viejo, J. Surface-Bulk Interplay in Vapor-Deposited Glasses: Crossover Length and the Origin of Front Transformation. *Phys. Rev. Lett.* **2019**, *123* (15), 155501. https://doi.org/10.1103/PhysRevLett.123.155501.

(9) Wang, L.; Ninarello, A.; Guan, P.; Berthier, L.; Szamel, G.; Flenner, E. Low-Frequency Vibrational Modes of Stable Glasses. *Nat. Commun.* **2019**, *10* (1), 26. https://doi.org/10.1038/s41467-018-07978-1.

(10) Seoane, B.; Reid, D. R.; de Pablo, J. J.; Zamponi, F. Low-Temperature Anomalies of a Vapor Deposited Glass. *Phys. Rev. Mater.* **2018**, *2* (1), 015602. https://doi.org/10.1103/PhysRevMaterials.2.015602.

(11) Angell, C. A. On the Uncertain Distinction between Fast Landscape Exploration and Second Amorphous Phase (Ideal Glass) Interpretations of the Ultrastable Glass Phenomenon. *J. Non. Cryst. Solids* **2015**, *407*, 246–255. https://doi.org/10.1016/j.jnoncrysol.2014.08.044.

(12) Lüttich, M.; Giordano, V. M.; Le Floch, S.; Pineda, E.; Zontone, F.; Luo, Y.; Samwer, K.; Ruta, B. Anti-Aging in Ultrastable Metallic Glasses. *Phys. Rev. Lett.* **2018**, *120* (13), 135504. https://doi.org/10.1103/PhysRevLett.120.135504.

(13) Khomenko, D.; Scalliet, C.; Berthier, L.; Reichman, D. R.; Zamponi, F. Depletion of Two-Level Systems in Ultrastable Computer-Generated Glasses. *Phys. Rev. Lett.* **2020**, *124* (22), 225901. https://doi.org/10.1103/PhysRevLett.124.225901.

(14) Perez-Castaneda, T.; Rodriguez-Tinoco, C.; Rodriguez-Viejo, J.; Ramos, M. A. Suppression of Tunneling Two-Level Systems in Ultrastable Glasses of Indomethacin. *Proc. Natl. Acad. Sci.* **2014**, *111* (31), 11275–11280. https://doi.org/10.1073/pnas.1405545111.

(15) Yu, H. B.; Tylinski, M.; Guiseppi-Elie, A.; Ediger, M. D.; Richert, R. Suppression of β Relaxation in Vapor-Deposited Ultrastable Glasses. *Phys. Rev. Lett.* **2015**, *115* (18). https://doi.org/10.1103/PhysRevLett.115.185501.

(16) Yu, H. Bin; Luo, Y.; Samwer, K. Ultrastable Metallic Glass. *Adv. Mater.* **2013**, *25* (41), 5904–5908. https://doi.org/10.1002/adma.201302700.

(17) Aji, D. P. B.; Hirata, A.; Zhu, F.; Pan, L.; Reddy, K. M.; Song, S.; Liu, Y.; Fujita, T.; Kohara, S.; Chen, M. Ultrastrong and Ultrastable Metallic Glass. *Prepr. arXiv1306.1575* **2013**.

(18) Guo, Y.; Morozov, A.; Schneider, D.; Chung, J. W.; Zhang, C.; Waldmann, M.; Yao, N.; Fytas, G.; Arnold, C. B.; Priestley, R. D. Ultrastable Nanostructured Polymer Glasses. *Nat. Mater.* **2012**, *11* (4), 337–343. https://doi.org/10.1038/nmat3234.

(19) Singh, S.; Ediger, M. D.; de Pablo, J. J. Ultrastable Glasses from in Silico Vapour Deposition. *Nat. Mater.* **2013**, *12* (2), 139–144. https://doi.org/10.1038/nmat3521.

(20) Kearns, K. L.; Swallen, S. F.; Ediger, M. D.; Wu, T.; Yu, L. Influence of Substrate Temperature on the Stability of Glasses Prepared by Vapor Deposition. *J. Chem. Phys.* **2007**, *127* (15), 154702. https://doi.org/10.1063/1.2789438.

(21) Kearns, K. L.; Swallen, S. F.; Ediger, M. D.; Wu, T.; Sun, Y.; Yu, L. Hiking down the Energy Landscape: Progress Toward the Kauzmann Temperature via Vapor Deposition. *J. Phys. Chem. B* **2008**, *112* (16), 4934–4942. https://doi.org/10.1021/jp7113384.

(22) Berthier, L.; Charbonneau, P.; Flenner, E.; Zamponi, F. Origin of Ultrastability in Vapor-Deposited Glasses. *Phys. Rev. Lett.* **2017**, *119* (18), 188002. https://doi.org/10.1103/PhysRevLett.119.188002.

(23) Sun, Q.; Miskovic, D. M.; Laws, K.; Kong, H.; Geng, X.; Ferry, M. Transition towards Ultrastable Metallic Glasses in Zr-Based Thin Films. *Appl. Surf. Sci.* **2020**, *533*, 147453. https://doi.org/10.1016/j.apsusc.2020.147453.

(24) Luo, P.; Cao, C. R.; Zhu, F.; Lv, Y. M.; Liu, Y. H.; Wen, P.; Bai, H. Y.; Vaughan, G.; di Michiel, M.; Ruta, B.; Wang, W. H. Ultrastable Metallic Glasses Formed on Cold Substrates. *Nat. Commun.* **2018**, *9* (1), 1389. https://doi.org/10.1038/s41467-018-03656-4.

(25) Bokas, G. B.; Zhao, L.; Morgan, D.; Szlufarska, I. Increased Stability of CuZrAl

Metallic Glasses Prepared by Physical Vapor Deposition. *J. Alloys Compd.* **2017**, *728*, 1110–1115. https://doi.org/10.1016/j.jallcom.2017.09.068.

(26) Jang, J.; Yoo, B.-G.; Kim, Y.-J.; Oh, J.-H.; Choi, I.-C.; Bei, H. Indentation Size Effect in Bulk Metallic Glass. *Scr. Mater.* **2011**, *64* (8), 753–756. https://doi.org/10.1016/j.scriptamat.2010.12.036.

(27) Lu, Y. M.; Sun, B. A.; Zhao, L. Z.; Wang, W. H.; Pan, M. X.; Liu, C. T.; Yang, Y. Shear-Banding Induced Indentation Size Effect in Metallic Glasses. *Sci. Rep.* **2016**, *6* (1), 28523. https://doi.org/10.1038/srep28523.

(28) Chu, J. P.; Jang, J. S. C.; Huang, J. C.; Chou, H. S.; Yang, Y.; Ye, J. C.; Wang, Y. C.; Lee, J. W.; Liu, F. X.; Liaw, P. K.; Chen, Y. C.; Lee, C. M.; Li, C. L.; Rullyani, C. Thin Film Metallic Glasses: Unique Properties and Potential Applications. *Thin Solid Films* **2012**, *520* (16), 5097–5122. https://doi.org/10.1016/j.tsf.2012.03.092.

(29) Liu, F. X.; Gao, Y. F.; Liaw, P. K. Rate-Dependent Deformation Behavior of Zr-Based Metallic-Glass Coatings Examined by Nanoindentation. *Metall. Mater. Trans. A* **2008**, *39* (8), 1862–1867. https://doi.org/10.1007/s11661-007-9399-8.

(30) Oliver, W. C.; Pharr, G. M. An Improved Technique for Determining Hardness and Elastic Modulus Using Load and Displacement Sensing Indentation Experiments. *J. Mater. Res.* **1992**, *7* (6), 1564–1583. https://doi.org/10.1557/JMR.1992.1564.

(31) Zhu, F.; Hirata, A.; Liu, P.; Song, S.; Tian, Y.; Han, J.; Fujita, T.; Chen, M. Correlation between Local Structure Order and Spatial Heterogeneity in a Metallic Glass. *Phys. Rev. Lett.* **2017**, *119* (21). https://doi.org/10.1103/PhysRevLett.119.215501.

(32) Barbee, T. W.; Walmsley, R. G.; Marshall, A. F.; Keith, D. L.; Stevenson, D. A. Phase Separation in Vapor Quench Synthesized Noncrystalline Copper Zirconium Alloys. *Appl. Phys. Lett.* **1981**, *38* (3), 132–135. https://doi.org/10.1063/1.92275.

(33) Kim, D. H.; Kim, W. T.; Park, E. S.; Mattern, N.; Eckert, J. Phase Separation in Metallic Glasses. *Progress in Materials Science*. Elsevier Ltd 2013, pp 1103–

1172. https://doi.org/10.1016/j.pmatsci.2013.04.002.

(34) Takeuchi, A.; Inoue, A. Classification of Bulk Metallic Glasses by Atomic Size Difference, Heat of Mixing and Period of Constituent Elements and Its Application to Characterization of the Main Alloying Element. *Mater. Trans.* **2005**, *46* (12), 2817–2829. https://doi.org/10.2320/matertrans.46.2817.

(35) Liu, Y. H.; Fujita, T.; Hirata, A.; Li, S.; Liu, H. W.; Zhang, W.; Inoue, A.; Chen, M. W. Deposition of Multicomponent Metallic Glass Films by Single-Target Magnetron Sputtering. *Intermetallics* **2012**, *21* (1), 105–114. https://doi.org/10.1016/j.intermet.2011.10.007.

(36) Jiang, H.; Xu, J.; Zhang, Q.; Yu, Q.; Shen, L.; Liu, M.; Sun, Y.; Cao, C.; Su, D.; Bai, H.; Meng, S.; Sun, B.; Gu, L.; Wang, W. Direct Observation of Atomic-Level Fractal Structure in a Metallic Glass Membrane. *Sci. Bull.* **2021**, No. 2020. https://doi.org/10.1016/j.scib.2021.02.020.

(37) Iwashita, T.; Nicholson, D. M.; Egami, T. Elementary Excitations and Crossover Phenomenon in Liquids. *Phys. Rev. Lett.* **2013**, *110* (20), 205504. https://doi.org/10.1103/PhysRevLett.110.205504.

(38) Basuki, S. W.; Bartsch, A.; Yang, F.; Rätzke, K.; Meyer, A.; Faupel, F. Decoupling of Component Diffusion in a Glass-Forming Zr46.75Ti8.25Cu7.5Ni10Be27.5 Melt Far above the Liquidus Temperature. *Phys. Rev. Lett.* **2014**, *113* (16), 165901. https://doi.org/10.1103/PhysRevLett.113.165901.

(39) Dziuba, T.; Luo, Y.; Samwer, K. Local Mechanical Properties of an Ultrastable Metallic Glass. *J. Phys. Condens. Matter* **2020**, *32* (34), 345101. https://doi.org/10.1088/1361-648X/ab8aa2.

(40) Liu, T.; Exarhos, A. L.; Alguire, E. C.; Gao, F.; Salami-Ranjbaran, E.; Cheng, K.; Jia, T.; Subotnik, J. E.; Walsh, P. J.; Kikkawa, J. M.; Fakhraai, Z. Birefringent Stable Glass with Predominantly Isotropic Molecular Orientation. *Phys. Rev. Lett.* **2017**, *119* (9), 095502. https://doi.org/10.1103/PhysRevLett.119.095502.

(41) Luo, P.; Li, M. X.; Jiang, H. Y.; Zhao, R.; Zontone, F.; Zeng, Q. S.; Bai, H. Y.; Ruta, B.; Wang, W. H. Nonmonotonous Atomic Motions in Metallic Glasses.

Phys. Rev. B **2020**, *102* (5), 054108. https://doi.org/10.1103/PhysRevB.102.054108.

(42) Juhás, P.; Farrow, C. L.; Yang, X.; Knox, K. R.; Billinge, S. J. L. Complex Modeling: A Strategy and Software Program for Combining Multiple Information Sources to Solve Ill Posed Structure and Nanostructure Inverse Problems. *Acta Crystallogr. Sect. A Found. Adv.* **2015**, *71* (6), 562–568. https://doi.org/10.1107/S2053273315014473.

(43) Sun, B. B.; Wang, Y. B.; Wen, J.; Yang, H.; Sui, M. L.; Wang, J. Q.; Ma, E. Artifacts Induced in Metallic Glasses during TEM Sample Preparation. *Scr. Mater.* **2005**, *53* (7), 805–809. https://doi.org/10.1016/j.scriptamat.2005.06.007.

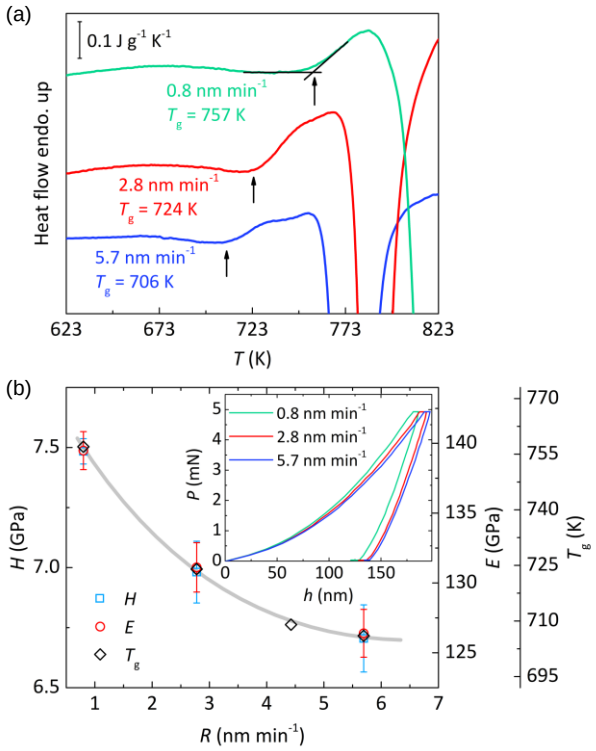

494

495 **Figure 1.** (a) DSC scans measured at 20 K min^{-1} for $Zr_{46}Cu_{46}Al_8$ MGs deposited at

496 different rates (*R*). (b) Hardness (*H*), modulus (*E*) and T_g as a function of *R*, the line is

497 guide to the eye. Inset: Representative nanoindentation load-depth (*P*-*h*) curves.

498

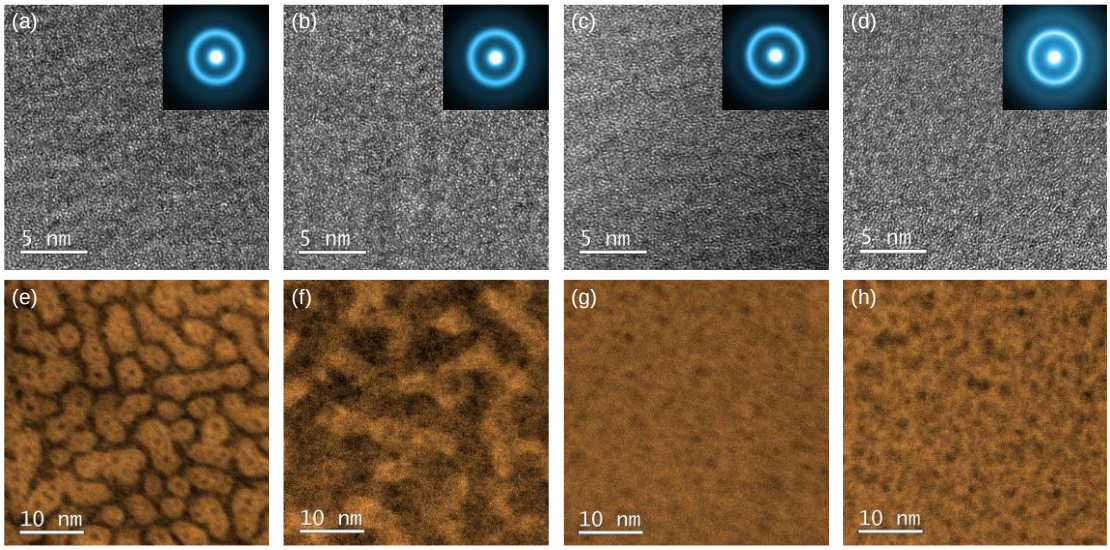

Figure 2. (a-d) HRTEM and (e-h) HAADF-STEM images of the MGs deposited at 5.7 nm min^{-1} (a,e), 2.8 nm min^{-1} (b,f) and 0.8 nm min^{-1} (c,g), and the liquid-quenched MG (d,h) for comparison. Insets in (a-d): SAED patterns.

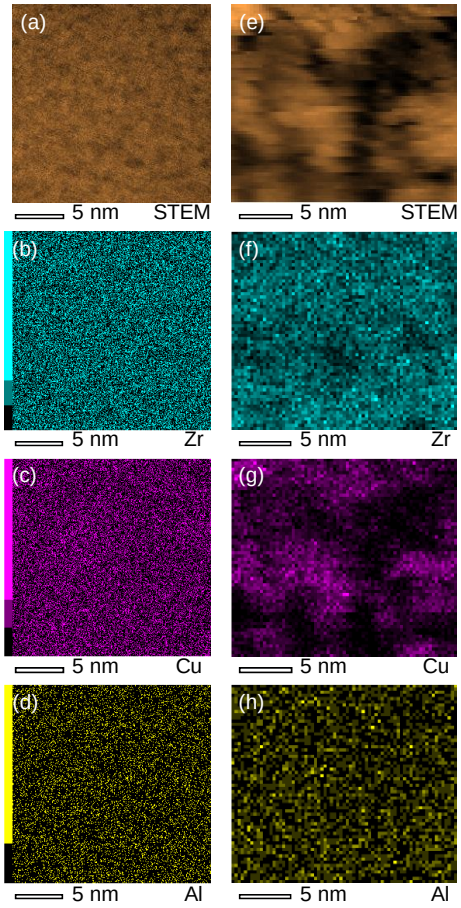

Figure 3. EDS mapping of the MGs deposited at 0.8 nm min^{-1} (a-d) and at 5.7 nm min^{-1} (e-h). Two different Cs-STEM instruments were used for the EDS mapping of the two samples (see detailed explanation in Experimental Methods).

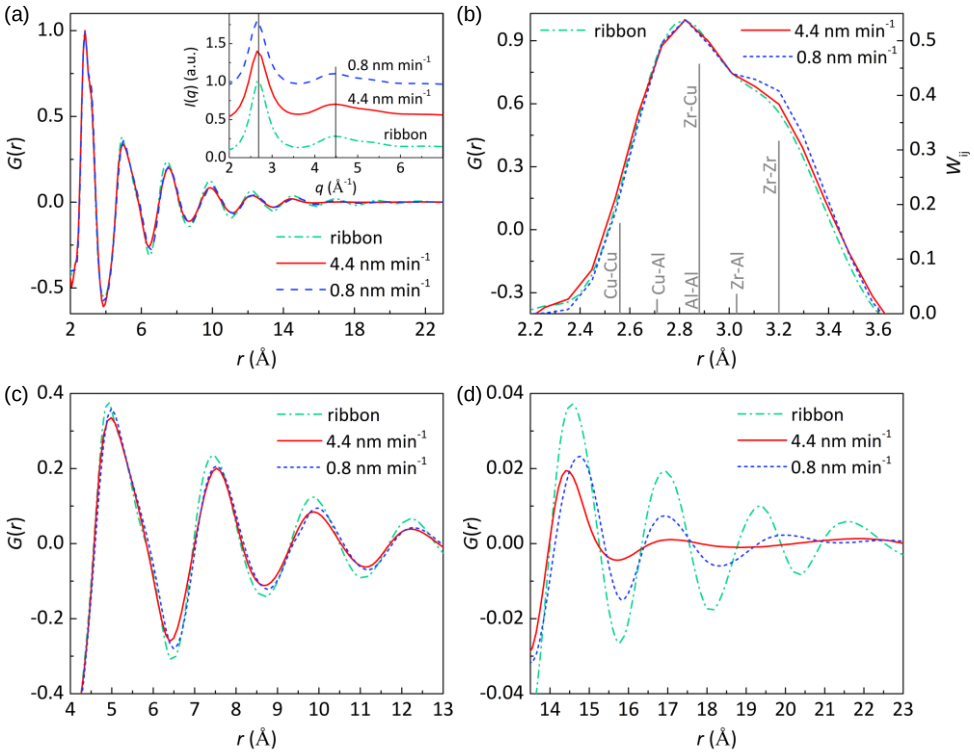

Figure 4. (a) Pair distribution functions $G(r)$ for MGs deposited at 4.4 nm min^{-1} and 0.8 nm min^{-1}, and liquid-quenched MG ribbon for comparison. Inset: Synchrotron XRD patterns, the vertical lines denote the peak position of liquid-quenched MGs. (b–d) Close-up views of the first (b), the second to the fifth (c), the sixth and later peaks of $G(r)$ (d). The vertical bars in (b) indicate the weight factors of atomic pairs W_{ij}.